

GRAVITATIONAL LENSING STATISTICS IN UNIVERSES DOMINATED BY DARK ENERGY

MICHAEL KUHLEN¹, CHARLES R. KEETON^{2,3}, & PIERO MADAU¹

submitted to ApJ

ABSTRACT

The distribution of image separations in multiply-imaged gravitational lens systems can simultaneously constrain the core structure of dark matter halos and cosmological parameters. We study lens statistics in flat, low-density universes with different equations of state $w = p_Q/\rho_Q$ for the dark energy component. The fact that dark energy modifies the distance-redshift relation and the mass function of dark matter halos leads to changes in the lensing optical depth as a function of image separation $\Delta\theta$. Those effects must, however, be distinguished from effects associated with the structure of dark matter halos. Baryonic cooling causes galaxy-mass halos to have different central density profiles than group- and cluster-mass halos, which causes the distribution of normal arcsecond-scale lenses to differ from the distribution of “wide-separation” ($\Delta\theta \gtrsim 4''$) lenses. Fortunately, the various parameters related to cosmology and halo structure have very different effects on the overall image separation distribution: (1) the abundance of wide-separation lenses is extremely sensitive (by orders of magnitude) to the distribution of “concentration” parameters for massive halos modeled with the Navarro-Frenk-White profile; (2) the transition between normal and wide-separation lenses depends mainly on the mass scale where baryonic cooling ceases to be efficient; and (3) dark energy has effects at all image separation scales. While current lens samples cannot usefully constrain all of the parameters, ongoing and future imaging surveys should discover hundreds or thousands of lenses and make it possible to disentangle the various effects and constrain all of the parameters simultaneously. Incidentally, we mention that for the sake of discovering lensed quasars, survey area is more valuable than depth.

Subject headings: cosmological parameters — cosmology: theory — dark matter — galaxies: halos — gravitational lensing

1. INTRODUCTION

Cold dark matter (CDM) theory makes robust predictions on the number density, spatial distribution, and structural properties of dark matter halos that must be compared with observational data to test the CDM paradigm. Given a large well-defined sample of strong gravitational lens systems, the distribution of image separations $\Delta\theta$ is a powerful and direct probe of the halo mass function and inner density profiles. This probe is attractive for being independent of the uncertainties about the relation between mass and luminosity that plague most astrophysical tools. As an example, the statistics of wide-separation ($\Delta\theta \gtrsim 6''$) lenses constrain the core mass fraction of dark matter halos on group and cluster mass scales, which depends on the “concentration” and slope of the central density cusp (Keeton & Madau 2001; also see Flores & Primack 1996), both of which are still uncertain and controversial (Navarro, Frenk, & White 1997; Moore et al. 1999; Jing & Suto 2000; Ghigna et al. 2000). On smaller, galaxy mass scales (corresponding to $\Delta\theta$ of a few arcseconds), the test is complicated by the presence of cooled baryons; when baryons cool and condense into a galaxy they modify the surrounding dark matter halo (e.g., Blumenthal et al. 1986).

The statistics of gravitational lensing are also sensitive to cosmological parameters, since these determine the

angular diameter distances to the lens and the source, and the number density of lens galaxies. Observations of distant Type Ia supernovae (Riess et al. 2001; Perlmutter et al. 1999), combined with measurements of cosmic microwave background (CMB) anisotropies (e.g., Spergel et al. 2003; de Bernardis et al. 2002; Pryke et al. 2002; Balbi et al. 2000), provide strong evidence that the dominant component in the universe — the exotic dark energy — is not associated with matter, has negative pressure, and is causing the cosmic expansion to accelerate. While several independent techniques appear to have converged rather tightly on a “concordance” model with parameters $\Omega_{\text{tot}} = 1$, $\Omega_M = 0.3$, $h = 0.7$, and $n = 1$, determining the equation of state of the dark energy remains one of the greatest challenges in cosmology and physics today. This may prove difficult with supernovae data alone (Gerke & Efstathiou 2002; Efstathiou 1999; Perlmutter, Turner, & White 1999), and additional observations (like CMB anisotropies, see e.g. Frieman et al. 2002) may be required to determine the nature of the negative pressure component.

Gravitational lensing statistics have already been used as another probe of the cosmic equation of state (Cooray & Huterer 1999; Waga & Friemann 2000; Sarbu, Rusin, & Ma 2001; Chae et al. 2002; Huterer & Ma 2003). Dark energy modifies the background cosmological line element, which affects the lensing geometry. It also modifies the power spectrum of density fluctuations on large scales (Ma et al. 1999), the rate of structure growth, the critical overdensity for spherical top-hat collapse, and the overdensity at virialization (Wang & Steinhardt 1998; Weinberg & Kamionkowski 2002), all of which affect the mass function and the internal structure of collapsed dark mat-

¹ Department of Astronomy and Astrophysics, University of California, 1156 High Street, Santa Cruz, CA 95064.

² Astronomy & Astrophysics Department, University of Chicago, 5640 S. Ellis Ave., Chicago, IL 60637.

³ Hubble Fellow.

ter halos, with consequences for the lensing cross section and the probability for multiple images. Because dark energy varies with redshift more slowly than matter, it starts contributing significantly to the expansion only relatively recently, at $z \lesssim 1$, where the lensing optical depth to distant quasars actually peaks.

In this paper we explore the ability of lens statistics to simultaneously constrain the core structure of dark matter halos, including both the concentration and the cooling mass scale, as well as the halo mass function and the cosmic equation of state. While other recent studies have examined various aspects of the problem, we consider all of the effects simultaneously to examine whether lensing can really distinguish between them, and whether lensed quasars can effectively be used to draw inferences on the background cosmology. The outline of the paper is as follows. We first present the ingredients of our calculations: the formalism for lens statistics (§2), and a description of structure formation under the influence of dark energy (§3). We then study how the various parameters in our model affect the results (§4). Next, we show that current lens data can test the model and constrain some of the parameters (§5). Finally, we argue that ongoing and future surveys should dramatically increase the samples of known lenses and provide powerful constraints on the parameters relating to dark energy and to the core structure of dark matter halos (§6). We offer our conclusions in §7.

2. LENSING METHODS

In this section we present the formalism for lens statistics calculations. In §2.1 we discuss the calculation of various lensing probability distributions. In §2.2 we describe our model for the internal structure of dark matter halos, in which halos corresponding to normal galaxies are treated as singular isothermal spheres (SIS), while lower and higher mass halos are assumed to have the Navarro-Frenk-White (1997, hereafter NFW) profile. In §§2.3–2.4 we review the lensing properties of SIS and NFW halos.

2.1. Probability calculations

We follow standard methods for computing lensing statistics (e.g., Narayan & White 1988; Kochanek 1995; Porciani & Madau 2000; Keeton & Madau 2001; Li & Ostriker 2002). Assume that the geometry of the universe is well approximated on large scales by the Friedmann-Robertson-Walker metric. Consider a population of objects that can act as deflectors, which lie at redshift z_l , have mass M , and may be characterized by a set of additional parameters \vec{p} (such as a “concentration” parameter as defined in §2.4). Let $dn/dM d\vec{p}$ be the differential comoving number density of deflectors with the specified properties. The differential probability that a point source at redshift z_s with flux S is lensed into multiple images by the deflector population is then (e.g., Turner, Ostriker, & Gott 1984)

$$\frac{dP}{dz dM d\vec{p}} = (1+z_l)^3 \frac{c dt}{dz} \frac{dn}{dM d\vec{p}} \times \sigma_L(z_s, z_l, M, \vec{p}) B(S; z_s, z_l, M, \vec{p}) \quad (1)$$

where

$$\frac{c dt}{dz} = \frac{c}{(1+z)H(z)} \quad (2)$$

is the cosmological line element, where $H \equiv \dot{a}/a$ is the Hubble parameter and $a = (1+z)^{-1}$ is the scale factor. In eq. (1), $\sigma_L(z_s, z_l, M, \vec{p})$ is the cross section for multiple imaging, and $B(S; z_s, z_l, M, \vec{p})$ is the “magnification bias” factor representing the fact that magnification causes lensed objects to be over-represented in flux-limited surveys.

The total lensing probability $P(z_s)$ can be computed by integrating eq. (1) over redshift, mass, and the additional deflector parameters \vec{p} . The distribution of lensing observables, such as the separation between the images, can be determined by inserting a selection function in the integral. For example, the probability of lensing with an image separation greater than $\Delta\theta$ is

$$P(>\Delta\theta; z_s) = \int dz_l dM d\vec{p} \frac{dP}{dz_l dM d\vec{p}} \mathcal{H}(\Delta\theta; z_s, z_l, M, \vec{p}), \quad (3)$$

where $\mathcal{H}(\Delta\theta; z_s, z_l, M, \vec{p})$ is unity if the parameters correspond to a lens with image separation greater than $\Delta\theta$, and zero otherwise. The probability of lensing with particular values of the time delay or the lens redshift can be computed in the analogous way.

We have computed the integrals with direct integration, and also with Monte Carlo methods where we sum the integrand for random values of the integration variables. The advantage of the Monte Carlo approach is the ability to compute the distributions of image separations, time delays, and lens redshifts simultaneously, but the disadvantage is the need for large-number realizations to reduce the statistical fluctuations in the results. We have verified that the two approaches produce equivalent results.

2.2. Overview of the model

The lensing cross section and magnification bias in eq. (1) depend on the radial density profile of the deflector. Two standard models for the density profile are the singular isothermal sphere (SIS) and the Navarro-Frenk-White (1997, hereafter NFW) profile. We cannot simply choose one or the other, however. Assuming that all massive objects have the same profile (be it SIS or NFW) produces a distribution of lensed image separations that is grossly inconsistent with the data at $\Delta\theta \sim 1''\text{--}10''$ (Flores & Primack 1996; Keeton 1998; Porciani & Madau 2000; Li & Ostriker 2002). The simplest model that agrees with the data has all objects below some mass M_{cool} assumed to be SIS, and all halos above M_{cool} assumed to be NFW. The transition from SIS to NFW is not ad hoc, but rather motivated by baryonic cooling. In large halos the baryons have not had time to cool so the systems retain their initial NFW form; while in small halos the gas has been able to cool, sink to the center of the halo, and create a more concentrated profile that can be approximated as SIS (Kochanek & White 2001). The lens data require a mass threshold $M_{\text{cool}} \sim 10^{13} h^{-1} M_\odot$, which is consistent with the halo mass whose cooling time equals the age of the universe, and also represents the mass scale of the transition from galaxies to groups and clusters.

Recently Li & Ostriker (2002) and Ma (2003) pointed out that similar arguments also apply on the small-separation and low-mass end: there must be a transition from SIS back to NFW (or a related form) as the mass

is decreased from normal galaxies ($\sim 10^{12} M_\odot$) down to dwarfs. This transition reflects the possibility that feedback effects or reionization could lead to a suppression of baryonic collapse in low-mass halos (Springel & Hernquist 2003; Bullock, Kravtsov, & Weinberg 2002)

We adopt the two-transition-mass approach, where halos below mass M_d (“dwarfs”) have NFW profiles, halos between M_d and M_c have SIS profiles, and halos above M_c (“clusters”) have NFW profiles. Some studies (e.g., Li & Ostriker 2002) have used generalized NFW profiles (Zhao 1996), where the central cusp is steeper than for NFW, for dwarfs. We always use the NFW form for simplicity, but our results should apply to models with steeper cusps as long as they have the same value of the core mass fraction (Keeton & Madau 2001). We consider only spherical halos because they are adequate for predicting the number of lenses (e.g., Keeton, Kochanek, & Seljak 1997; Chae 2002).

2.3. SIS lens

There is now strong evidence that the mass distributions of early-type galaxies within several optical radii are well described by the SIS profile; the evidence comes from lensing (Cohn et al. 2001; Rusin, Kochanek, & Keeton 2003), X-rays (Fabbiano 1989), stellar dynamics (Rix et al. 1997), and even joint lensing and stellar dynamical analyses (Koopmans & Treu 2003; Treu & Koopmans 2003). An SIS halo has density profile $\rho = \sigma_v^2/(2\pi Gr^2)$, where σ_v is the velocity dispersion, which is related to the total mass M within the virial radius by

$$\sigma_v(M, z) = \frac{1}{2} H_0^2 r_0 \Omega_M^{1/2} \Delta_{\text{vir}}^{1/6} (1+z)^{1/2}. \quad (4)$$

Here $r_0 = (3M/4\pi\rho_0)^{1/3}$ is the comoving radius of the collapsing perturbation, z denotes the virialization epoch of the halo, and $\Delta_{\text{vir}}(z)$ is the virial overdensity of the halo (see §3.6). SIS models are fully described by the mass and redshift, so there are no additional parameters \vec{p} and the factor $dn/dM d\vec{p}$ in eq. (1) is just the mass function dn/dM .

An SIS lens has an angular Einstein radius

$$\theta_E = 4\pi \left(\frac{\sigma_v}{c}\right)^2 \frac{D_{ls}}{D_{os}}, \quad (5)$$

where D_{ls} and D_{os} are angular diameter distances from the lens to the source and observer to the source, respectively. The image separation is $\Delta\theta = 2\theta_E$, and the lensing cross section is $\sigma_{\text{SIS}}^* = \pi(\theta_E D_{ol})^2$ where D_{ol} is the angular diameter distance from the observer to the lens. The magnification bias is

$$B(S) = \frac{2}{\theta_E^2} \int_0^{\theta_E} dy y \frac{N(>S/\mu(y))}{N(>S)}, \quad (6)$$

where $N(>S)$ is the number of sources with flux greater than S . The magnification $\mu(y)$ can be the magnification of either of the two images ($\mu_\pm = \theta_E/y \pm 1$) or the total magnification ($\mu_{\text{tot}} = 2\theta_E/y$), depending on the details of a lens survey. For example, when studying the CLASS survey (§5) we use the total magnification because the targets in the initial catalog were unresolved. Combining this with a source luminosity function modeled as a power law $dN/dS \propto S^\nu$ would yield a magnification bias of $B = 2^{-\nu}/(3 + \nu)$.

2.4. NFW lens

High-resolution N -body simulations of the formation of dark matter halos consistently produce halo density profiles shallower than SIS in the core (NFW; Moore et al. 1999). NFW argue that the halos form a two-parameter family described by the density profile

$$\rho(r) = \frac{\rho_s}{(r/r_s)(1+r/r_s)^2}, \quad (7)$$

where ρ_s is a characteristic density and r_s is a scale radius. In many cases it is more convenient to take as the two free parameters the virial mass M and a “concentration” parameter $c = r_{\text{vir}}/r_s$. Note that some authors define the concentration as $c = r_{200}/r_s$, where r_{200} is the radius at which the mean density of the halo is equal to 200 times the critical density (NFW; Li & Ostriker 2002). This definition is independent of cosmology, whereas the definition in terms of the virial radius takes into account differences in the virial overdensity for different cosmologies (see §3.6)

The two parameters are not actually independent; Bullock et al. (2001) found that the concentration parameter follows a log-normal distribution where the median depends on the halo mass and redshift,

$$c_{\text{med}}(M, z) = \frac{\bar{c}_*}{1+z} \left(\frac{M}{M_*}\right)^\alpha, \quad (8)$$

where M_* is the mass of a typical halo collapsing today (see §3.4). Thus, for NFW halos we can write the factor $dn/dM d\vec{p}$ in eq. (1) as

$$\frac{dn}{dM d\log c} = \frac{dn}{dM} \frac{1}{\sqrt{2\pi} \sigma_{\log c}} \exp\left[-\frac{(\log c - \log c_{\text{med}})^2}{2\sigma_{\log c}^2}\right]. \quad (9)$$

The halos in the Λ CDM simulations by Bullock et al. were best described by $\alpha = -0.13$ and $\bar{c}_* = 9.0$, with a scatter around the median of $\sigma_{\log c} = 0.14$ dex. (Note that Bullock et al. (2001) incorrectly quote $\sigma_{\log c} = 0.18$ dex. This error has been corrected in Wechsler et al. (2002).) We find that at large separations the abundance of lenses is very sensitive to both \bar{c}_* and $\sigma_{\log c}$, so we treat both of them as model parameters. Other models for the concentration distribution have been discussed, but they generally agree out to $z \sim 1$ (Eke, Navarro, & Steinmetz 2001; Wechsler et al. 2002; Zhao et al. 2003a, 2003b).

Bartelmann (1996) derives the lensing properties of NFW halos, and Oguri et al. (2002) give useful analytic approximations for the image separation and magnification. The lens equation has the form

$$y = x - \mu_s \frac{g(x)}{x}, \quad (10)$$

where x is the magnitude of the position vector in the lens plane, scaled by r_s , and y the magnitude of the position vector in the source plane, scaled by $r_s D_{ol}/D_{os}$. The lensing efficiency is parameterized by $\mu_s = 4\rho_s r_s / \Sigma_{\text{cr}}$, where

$$\Sigma_{\text{cr}} = \frac{c^2}{4\pi G} \frac{D_{os}}{D_{ol} D_{ls}} \quad (11)$$

is the critical surface mass density for lensing (Turner et al. 1984). Lastly,

$$g(x) \equiv 2 \int_0^x \frac{\Sigma(x')}{\Sigma_{\text{cr}}} x' dx', \quad (12)$$

which for the NFW profile evaluates to:

$$g(x) = \ln \frac{x}{2} + \begin{cases} \frac{1}{\sqrt{1-x^2}} \operatorname{arctanh} \sqrt{1-x^2}, & 0 < x < 1, \\ 1, & x = 1, \\ \frac{1}{\sqrt{x^2-1}} \arctan \sqrt{x^2-1}, & x > 1. \end{cases} \quad (13)$$

The Einstein radius x_E of the lens is the root of $y(x)$. The ‘‘radial critical radius’’ x_{cr} is the root of dy/dx . It maps to the radial caustic $y_{\text{cr}} = |y(x_{\text{cr}})|$. Any source with $|y| \leq y_{\text{cr}}$ is strongly lensed into three images with $|x_1| > |x_2| > |x_3|$. The image separation is $\Delta\theta = (|x_1| + |x_2|)r_s/D_{ol}$, so it depends on the source position $|y|$. However, Oguri et al. (2002) and Li & Ostriker (2002) argue that the separation is well approximated by $\Delta\theta \approx 2x_E r_s/D_{ol}$. We find that our results are indistinguishable when we use this approximation and when we use the exact image separation found by explicitly solving the lens equation. The lensing cross section is $\sigma_{\text{NFW}}^* = \pi(y_{\text{cr}} r_s)^2$, and the magnification bias is

$$B(S) = \frac{2}{y_{\text{cr}}^2} \int_0^{y_{\text{cr}}} dy y \frac{N(>S/\mu(y))}{N(>S)}, \quad (14)$$

where $N(>S)$ is the number of sources with flux greater than S , and $\mu(y)$ is the magnification of a source at impact parameter y . As in §2.3, the magnification may be that of either image or the total magnification, depending on the details of a lens survey. The magnification must be found by explicitly solving the lens equation and then using the fact that an image at position x has magnification $\mu = [y(x)/x]^{-1} [dy/dx]^{-1}$.

3. STRUCTURE FORMATION IN QCDM

In this section we summarize the main features of structure formation in a universe filled with dark matter and dark energy. For calculations of lens statistics, the quantities we need are the geometry of the universe (§3.1), the mass function of halos (§3.5) and the virial overdensity (§3.6).

While the nature of the dark energy remains unknown, a cosmological constant Λ or a dynamical scalar field called ‘‘quintessence’’ (Caldwell, Dave, and Steinhardt 1998; Peebles & Ratra 1988) are the most discussed candidates. The effective equation of state of the dark energy is usually parameterized as $w = p_Q/\rho_Q$, where $w = -1$ for a pure cosmological constant but may be larger for a scalar field component or smaller for phantom energy (Caldwell et al. 2003); w may be constant or time-varying. If w is assumed to be constant in time, the combined data sets from Type Ia supernovae (SNe) and the CMB or large-scale structure already imply $-1.30 \leq w \leq -0.6$ (Spergel et al. 2003; Baccigalupi et al. 2002; Wang et al. 2000). Our calculations apply to models with a constant or slowly varying equation of state (Steinhardt, Wang, & Zlatev 1999). We generically refer to dark energy as a ‘‘Q-component’’, and to cosmological models with a mixture of dark energy and cold dark matter (CDM) as QCDM. Λ CDM is then a special case of QCDM with $w = -1$.

3.1. Cosmography

In the limit of a nearly homogeneous Q-component, all the consequences of the Q-field follow from its effect on

the expansion rate:

$$\frac{H^2(z)}{H_0^2} = \Omega_M(1+z)^3 + \Omega_Q(1+z)^{3(1+w)} + \Omega_K(1+z)^2, \quad (15)$$

where H_0 is the Hubble parameter today, Ω_M and Ω_Q are the matter and dark energy density parameters today, and $\Omega_K = 1 - \Omega_M - \Omega_Q$ is the contribution of curvature. In an $\Omega_K = 0$ flat universe, the angular diameter distance from an object at redshift z_1 to an object at redshift z_2 is given by

$$D_A(z_1, z_2) = \frac{c}{1+z_2} \int_{z_1}^{z_2} \frac{dz}{H(z)}. \quad (16)$$

3.2. Linear growth of perturbations

In first-order perturbation theory, the growing-mode solution of the matter density contrast satisfies the differential equation

$$\ddot{D} + 2H(z)\dot{D} = \frac{3}{2}H_0^2\Omega_M(1+z)^3D, \quad (17)$$

where D is the linear growth factor and the dots denote derivatives with respect to time. An analytical solution in terms of hypergeometric functions can be found in Padmanabhan (2003). A good approximation to the instantaneous growth index $f = d \ln D / d \ln a$ as the matter density parameter $\Omega_M(z) = \Omega_M(1+z)^3(H_0^2/H^2)$ approaches unity is given by

$$f \approx \Omega_M(z)^{\frac{3-3w}{5-6w}} = \left[\frac{\rho_M(z)}{\rho_M(z) + \rho_Q(z)} \right]^{\frac{3-3w}{5-6w}}, \quad (18)$$

where ρ_Q and ρ_M are the Q-field and matter densities, respectively (Silveira & Waga 1994; Wang & Steinhardt 1998). We see that the growth of density perturbations is slowed as ρ_Q approaches ρ_M . Growth suppression increases with increasing w since the onset of dark energy domination occurs at higher redshift: in order to achieve the level of mass fluctuations observed today, cosmic structure in QCDM must form at earlier times (Huterer & Turner 2001).

3.3. Power spectrum

Dark halos form from primordial matter density fluctuations in the early universe. The Q-field is so light that on scales less than a few hundred Mpc fluctuations in Q disperse relativistically, and quintessence behaves as a smooth component like the cosmological constant. On very large scales, however, the dark energy may cluster gravitationally. Fluctuations in the Q-field add to the right-hand side of equation (17), resulting in a different growth rate once quintessence starts to dominate the cosmological energy density. This change of behavior is incorporated in the transfer function for the matter density field, which accounts for all modifications of the primordial power-law spectrum due to the effects of pressure and dissipative processes, together with the gravitational clustering of matter and dark energy. The linear power spectrum for matter density perturbations in QCDM scenarios can be expressed as

$$P(k, z; w) = Ak^n T_Q^2(k, z; w) \left[\frac{D(z; w)}{D_0} \right]^2, \quad (19)$$

where A is an overall normalization, k is the wavenumber, n is the spectral index of the post-inflationary adiabatic density perturbation, $T_Q(k, z; w)$ is the transfer function, and D is the growth factor from equation (17).

Ma et al. (1999) provide a prescription in which the modification due to quintessence with $w > -1$ are captured by a multiplicative factor $T_{Q\Lambda}(k, z)$ to be applied to the standard Λ CDM transfer function $T_\Lambda(k)$, i.e. $T_Q \equiv T_{Q\Lambda}T_\Lambda$. (The Λ CDM transfer function can be taken from, e.g., Eisenstein & Hu 1999.) In contrast to models with no dark energy ($\Omega_Q = 0$) or ones with a nonzero cosmological constant, ($\Omega_Q \neq 0$, $w = -1$), a Q-field with $\Omega_Q > 0$, $w > -1$ adds power to $P(k)$ at small wavenumbers, increasingly so as the contribution of quintessence to the energy density becomes larger. This effect introduces an additional dependence of the transfer function on redshift (Ma et al. 1999). At this time no such prescription for $w < -1$ phantom energy type models has been published. Fortunately the modifications to the Λ CDM transfer function are non-negligible only on scales comparable to the horizon. On the sub-cluster scales relevant for our calculations it is thus possible to ignore these effects.

3.4. Mass variance

On the scale of galaxy clusters and below, the QCDM power spectrum has identical shape to the Λ CDM one and differs only in the overall amplitude. To fix the normalization factor A in equation (19), we compute the variance of the mass-density field smoothed on a scale of comoving radius R ,

$$\sigma_M^2 = \langle (\delta M/M)^2 \rangle = \frac{1}{2\pi^2} \int_0^\infty dk k^2 P(k, z) W^2(kR), \quad (20)$$

where $M = H_0^2 \Omega_M R^3 / 2G$ is the mass inside a sphere of radius R , and $W(kR)$ is the Fourier transform of the spherical top-hat window function, $W(x) = (3/x^2)(\sin x/x - \cos x)$. For calculations of lensing by halos on the scale of clusters and smaller, it seems most appropriate to normalize the QCDM power spectrum by the local abundance of galaxy clusters.⁴ Although the normalization of a QCDM power spectrum by cluster abundances has been discussed by Wang & Steinhardt (1998), we present it in the Appendix since we use the more recent data set of Reiprich & Böhringer (2002). We find that the data favor a value of the rms mass fluctuations $8 h^{-1}$ Mpc spheres, $\sigma_8 \equiv \sigma(z=0, R=8 h^{-1} \text{ Mpc}) = 0.74$, for the currently favored cosmology with $\Omega_M = 0.3$, $\Omega_Q = 0.7$, $h = 0.7$, and $n = 1$, independently of w for $-1.5 < w < -0.5$ (see the Appendix for details). Then the normalization factor in eq. (19) is

$$A = \frac{2\pi^2 \sigma_8^2}{\int_0^\infty dk k^{n+2} T_Q^2(k, 0) W^2(kR_8)}. \quad (21)$$

Following Bullock et al. (2001) we define M_* as the mass of halos collapsing today from $1\text{-}\sigma$ fluctuations, i.e. as the solution of $\sigma_M = \delta_c$, where δ_c is the linearly extrapolated overdensity at collapse (see §3.6). Table 1

⁴ By contrast, Sarbu et al. (2001) compute lens statistics using a QCDM power spectrum normalized by the COBE measurement of the cosmic microwave background, corresponding to scales near the horizon scale today.

TABLE 1. $M_*(w)$ [$10^{12} M_\odot$]

σ_8	w				
	-0.50	-0.75	-1.00	-1.25	-1.50
0.74	3.71	3.58	3.52	3.47	3.44
0.90	11.9	11.5	11.3	11.2	11.1

shows M_* for various values of w , for our favored value of $\sigma_8 = 0.74$ and also for $\sigma_8 = 0.90$.

3.5. Halo mass function

The mass function of collapsed objects has been derived from theoretical arguments and from N -body simulations. The classic prediction comes from Press & Schechter (1974), and it has been adjusted by Sheth & Tormen (1999) to better fit results from simulations. Jenkins et al. (2001) have presented an alternate fitting form that they claim fits a wide variety of N -body simulations. The functional forms of these three models are:

$$n_{\text{PS}}(M) = -\sqrt{\frac{2}{\pi}} \frac{\rho_b}{M} \frac{\delta_c}{\sigma_M^2} \frac{d\sigma_M}{dM} \exp \left[-\frac{1}{2} \left(\frac{\delta_c}{\sigma_M} \right)^2 \right] \quad (22a)$$

$$n_{\text{ST}}(M) = -\frac{0.383}{\sqrt{\pi}} \frac{\rho_b}{M} \frac{\delta_c}{\sigma_M^2} \frac{d\sigma_M}{dM} \left[1 + \left(\frac{\sigma_M^2}{0.707\delta_c^2} \right)^{0.3} \right] \times \exp \left[-\frac{0.707}{2} \left(\frac{\delta_c}{\sigma_M} \right)^2 \right] \quad (22b)$$

$$n_{\text{J}}(M) = -\frac{\rho_0}{M} \frac{d\sigma_M}{dM} \frac{0.315}{\sigma_M} \exp \left[-|0.61 - \ln \sigma_M|^{3.8} \right] \quad (22c)$$

We adopt the Jenkins et al. mass function as our fiducial model, but we explore the effects of using the other approximations as well. While the original analysis by Jenkins et al. did not include any cases with $w \neq -1$, recent results from N -body simulations including the effect of a dark energy component with $w \neq -1$ confirm the validity of the fitting function (Linder & Jenkins 2003; Kuhlen et al., in preparation).

3.6. Spherical top-hat collapse

The PS and ST mass functions and the definition of M_* depend on the linearly extrapolated overdensity at collapse δ_c . The SIS and NFW halo lensing cross sections depend on the virial overdensity $\Delta_{\text{vir}} = (\rho/\rho_M)_{\text{vir}}$. Both δ_c and Δ_{vir} are determined by solving the spherical collapse model (e.g., Wang & Steinhardt 1998; Strigari 2003, private communication). While the changes in δ_c with w are only a few percent, the changes in Δ_{vir} are more noticeable. As w increases Δ_{vir} becomes larger as structures form earlier. At $z = 0$ we find $\Delta_{\text{vir}} = (499, 409, 346, 298, 270)$ for $w = (-0.50, -0.75, -1.00, -1.25, -1.50)$ (Strigari 2003, private communication). For $w \geq -1$ fitting formulae for both quantities have been published by Weinberg & Kamionkowski (2002).

TABLE 2. FIDUCIAL MODEL AND VARIATIONS

Parameter	Fiducial Value	Variation Values
Ω_m	0.3	–
Ω_q	0.7	–
w	–1.00	–0.50, –0.75, –1.25, –1.50
n	1.0	–
h	0.7	–
dn/dM	Jenkins	PS, ST
\bar{c}_*	9.0	6.5, 12.4
$\sigma_{\log c}$	0.14	0.21, 0.07, 0.00
$\log M_d$	0.0	12.0
$\log M_c$	13.50	13.25, 13.75
σ_{z_s}	0.0	0.2, 0.4, 0.6, VLBI

From the previous two sections it is clear that there are a number of parameters that enter into lens statistics calculations. In this section we study how they affect the results. Our goal is not to exhaustively catalog and quantify all parameter dependences and covariances, but to identify the main qualitative features. To do this, we adopt a fiducial model (which shall be justified in §5), and then vary the parameters one at a time. The fiducial model and the variations are summarized in Table 2. Figure 1 shows the optical depth as a function of source redshift, the image separation distribution, and the time delay distribution for the fiducial model. Figures 2–4 then show how the parameter variations affect the image separation distribution, the time delay distribution, and the lens redshift distribution.

Note that the image separation distributions are normalized so the total probability reflects the probability of lensing, while the time delay and lens redshift distributions are normalized so the total probability is unity. This allows us to separate changes in the overall lensing probability from changes in the shapes of the time delay and lens redshift distributions. Also note that in Figures 2 and 3 we plot the cumulative separation and time delay distributions, but for completeness in Figure 1 we show the differential distributions. Finally, note that the calculations in this section are designed for comparison with the CLASS survey: we use a source redshift distribution with mean $\langle z_s \rangle = 1.27$, and we compute magnification bias using the total magnification and a source luminosity function modeled as a power law $dN/dS \propto S^{-2.1}$ (see Rusin & Tegmark 2001; Browne et al. 2002).

4.1. The fiducial model

In our fiducial model, the image separation distribution peaks around $\Delta\theta \sim 1''\text{--}2''$, and has a long tail to small separations (see Fig. 1). Above the peak the distribution drops quickly, then has a kink at $\Delta\theta \sim 4''$ with a long but low-amplitude tail to large separations. This feature represents the transition from normal lenses produced by galaxies modeled as SIS halos, to wide-separation lenses produced by groups and clusters modeled as NFW halos. NFW halos are much less efficient lenses than SIS, so wide-separation lenses are much less abundant than normal arcsecond-scale lenses.

The time delay distribution is surprisingly broad, spanning more than three orders of magnitude (also see Oguri et al. 2002). Thus, in future surveys a substantial frac-

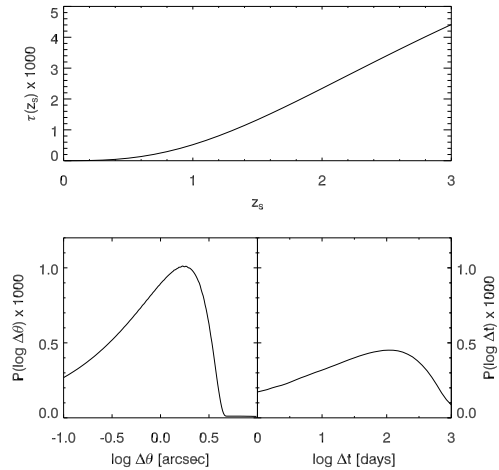


FIG. 1.— Lens statistics results for the fiducial model. (Top) The total lensing probability as a function of the source redshift. (Bottom) The image separation and time delay distributions.

tion of lenses will have time delays on week or month time scales for which measurements will be feasible, but a non-negligible fraction of lenses will have time delays that are too long to be of practical use. There is actually a kink in the time delay distribution marking the transition from normal to wide-separation lenses, but it occurs at ~ 1100 days and is not visible in Figure 1.

4.2. Variation in w

As discussed in §3, the fact that dark energy modifies cosmological dynamics is taken into account self-consistently in everything except for the effect on the NFW concentration parameter. Since overdensities collapse earlier as w increases, the median concentration should increase with w . Some analytical and numerical studies of halo concentrations in universes with $w \neq -1$ have been made (Bartelmann, Perrotta, & Baccigalupi 2003; Klypin et al. 2003; Kuhlen et al. , in preparation), but so far no $\bar{c}_*(w)$ relations have been published. The explicit w dependence of $\bar{c}_*(w)$ appears to be rather small, certainly less than the scatter $\sigma_{\log c}$, so we neglect it in this work.

Figure 2 shows that changing w affects the full range of image separations. The effects are largest at wide separations ($\Delta\theta \gtrsim 4''$), with more than twice as many lenses for $w = -0.50$ as for Λ CDM. This makes sense, because wide-separation lenses are produced by massive group and cluster halos, which are more abundant at redshifts $z_l \sim 0.2\text{--}1$ in models with larger w by virtue of the earlier structure formation. Increasing w slightly decreases the number of lenses with $\Delta\theta \lesssim 2''$; among the parameters we examine, this is the main change at arcsecond scales. An increase in w also shifts the time delay distribution to slightly higher values (Fig. 3), and shifts the lens redshift distribution to slightly lower values (Fig. 4).

We conclude that wide-separation lenses can be used to place useful constraints on w only after parameters governing the abundance and structure of massive halos ($\sigma_8, \bar{c}_*, \sigma_{\log c}, M_c$) are much better constrained (cf. Sarbu et al. 2001). Normal arcsecond-scale lenses can provide more robust constraints on w , but large future samples

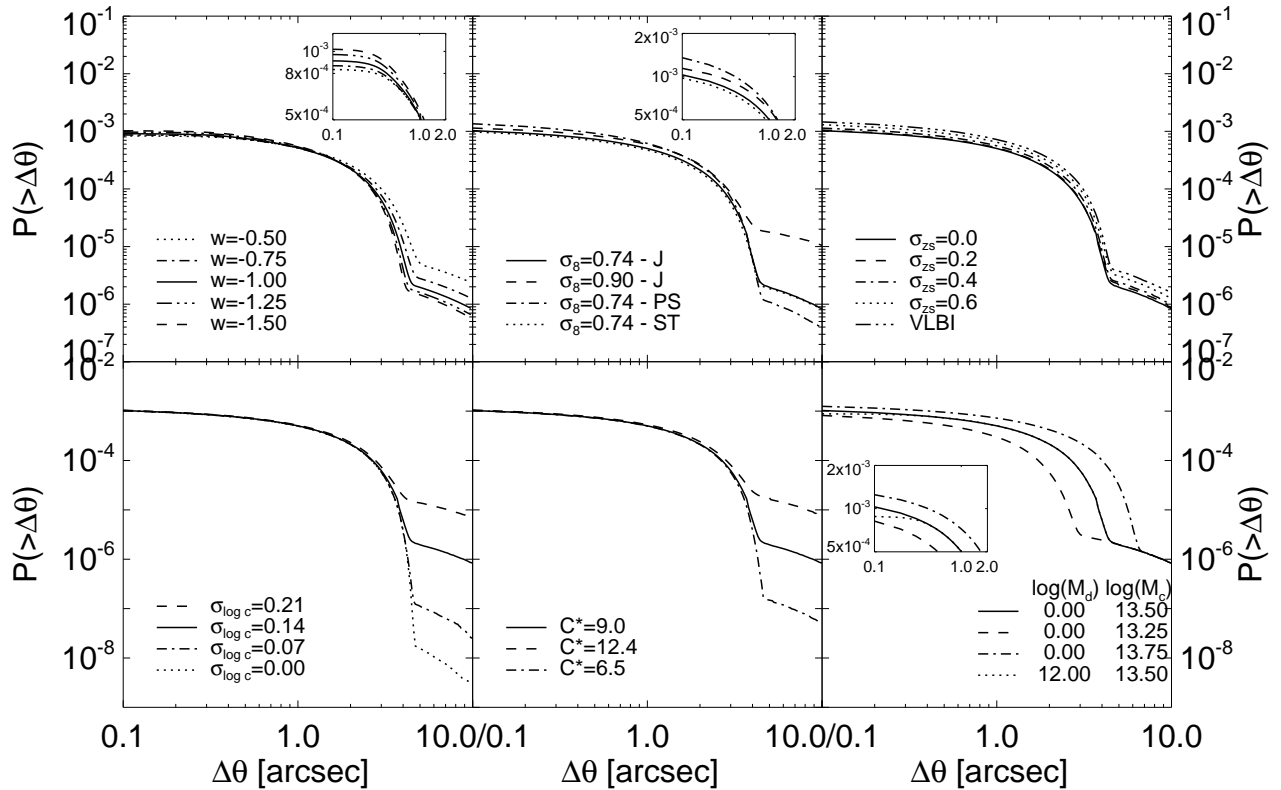


FIG. 2.— The effects of parameter variations on the cumulative distribution of image separations.

will be needed to detect the relatively weak effects of w . In this regard our results differ from those of Huterer & Ma (2003), who claim an upper limit $w < -0.85$ at 68% confidence using the current CLASS lens sample.

4.3. Variation in the mass function and σ_8

The strongest effect in this group comes from changes in σ_8 . In order to match the observed abundance of clusters from HIFLUGCS we have adopted a low value $\sigma_8 = 0.74$. Determinations of σ_8 at much larger scales (COBE, WMAP, weak lensing, excess power in CMB at $l > 1000$, etc.; Ma et al. 1999; Spergel et al. 2003; Huterer & White 2002; Komatsu & Seljak 2002), by contrast, tend to favor a higher value $\sigma_8 \sim 0.90$. At present there exists no satisfying reconciliation of this tension, so we are forced to treat σ_8 as an unknown. The seemingly small increase in σ_8 from 0.74 to 0.90 produces a change of about an order of magnitude in the abundance of wide-separation lenses. The total lensing probability, however, is affected by only 10%. The increased abundance of wide-separation lenses, which have long time delays, shifts the time delay distribution to slightly higher values.

The use of different mass functions, Press–Schechter vs. Sheth–Tormen vs. Jenkins, produces a smaller effect. The PS mass function tends to over- (under-) predict the abundance of halos below (above) $\sim 10^{14} M_\odot$ relative to N -body simulations, while the ST and Jenkins mass functions both aim to correct this problem. Thus

it is not surprising to see that the PS mass function tends to predict more small-separation lenses and fewer large-separation lenses than the ST/J mass functions. Relative to the Jenkins mass function, the ST mass function produces slightly fewer lenses at all separations, but the differences are less than 10%. The tendency for the PS and ST to shift the image separation distribution to lower values also shifts the time delay distribution to lower values; the shift in the median is 17% for ST and 25% for PS.

4.4. Variation in source distribution

Our fiducial model assumes that all sources lie at redshift $z_s = 1.27$, but we consider several other possibilities as follows. First, we consider Gaussian distributions with the same mean but different widths σ_{z_s} . Second, we consider using the source redshift distribution from the 2nd Caltech/Jodrell Bank VLBI sample (Henstock et al. 1997). This distribution is reasonably well described by a Gaussian with mean $\langle z_s \rangle = 1.33$ and width $\sigma_{z_s} = 0.75$, but we use the actual observed distribution. This is the same redshift distribution used by Sarbu, Rusin, & Ma (2001) in their study of the effects of dark energy on strong lensing.

Figure 2 shows that with the mean source redshift fixed, increasing the scatter even to $\sigma_{z_s} \sim 0.4$ has little effect on the optical depth or image separation distribution. Only when the scatter reaches $\sigma_{z_s} \sim 0.6$ is there a notable increase, which is due to the growing number

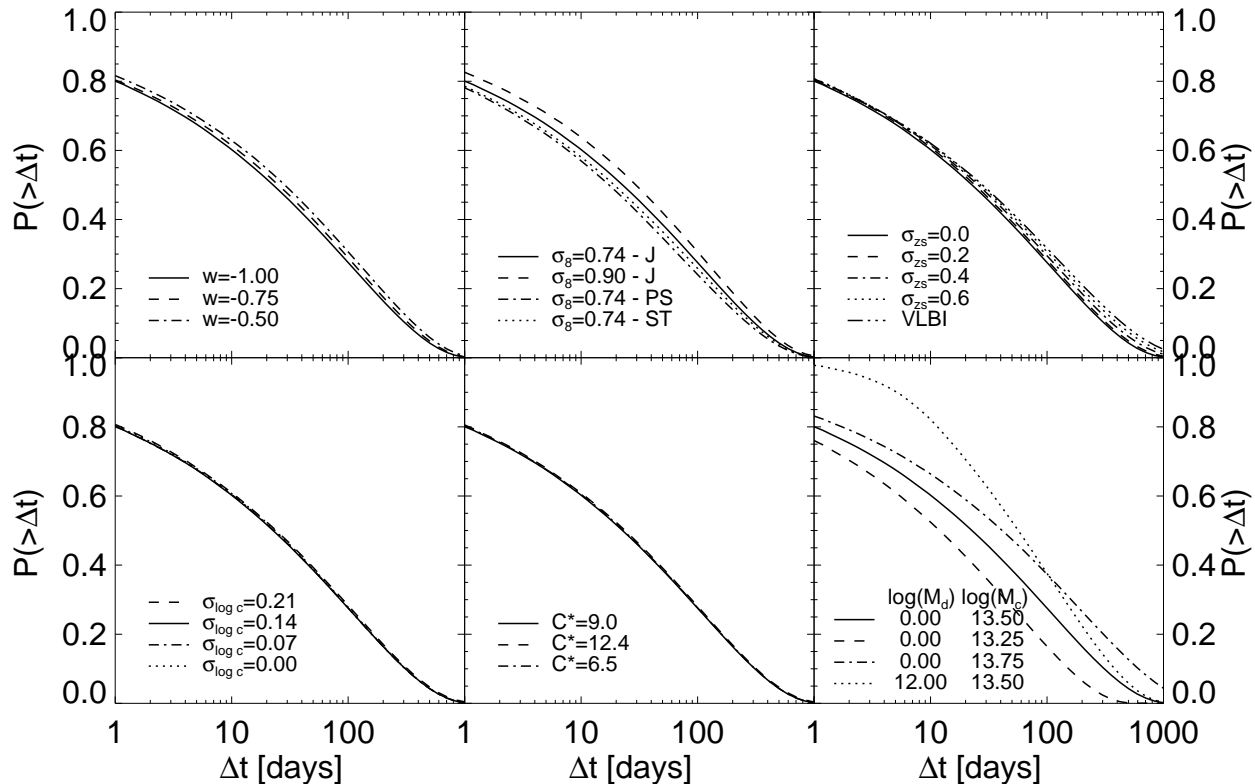


FIG. 3.— The effects of parameter variations on the normalized cumulative distribution of time delays.

of sources at higher redshifts (where the optical depth is higher). The higher optical depth for the model with the VLBI redshift distribution ($\sim 40\%$ higher than for the fiducial model) is due partly to the higher mean redshift and partly to the large width of the distribution. Not surprisingly, broadening the source redshift distribution causes the lens redshift distribution to show a larger tail to higher redshifts.

4.5. Variation in \bar{c}_* and $\sigma_{\log c}$

The parameters \bar{c}_* and $\sigma_{\log c}$ control the distribution of concentration parameters for NFW halos. They have little effect on arcsecond-scale lenses because those are produced by galaxies with roughly isothermal profiles. But they have an enormous effect on the abundance of wide-separations lenses produced by group and cluster halos. Increasing the median concentration \bar{c}_* by 0.14 dex (the 1σ scatter found by Bullock et al. 2001) increases the abundance of wide-separation lenses by more than a factor of 8, while decreasing \bar{c}_* by 0.14 dex decreases the abundance by a factor of ~ 15 . Even more extreme is the effect of changing the scatter in the $c(M, z)$ relation. Neglecting the scatter (using $\sigma_{\log c} = 0$) reduces the abundance of wide-separation lenses by more than two(!) orders of magnitude. Both effects are explained by the fact that making a halo less concentrated can dramatically reduce its lensing cross section and its ability to produce lenses of a given size. This, of course, was the original reason for using NFW halos in lens statis-

tics: halos that are less concentrated than SIS are needed to explain the lack of observed wide-separation lenses.

It is important to understand this result in more detail. In Figure 5 we show how varying the concentration (for fixed mass and redshift) affects the lensing properties of an NFW halo. Panel (b) shows a log-normal distribution of concentrations with width $\sigma_{\log c} = 0.14$ dex. Panel (c) shows the corresponding distribution of the lensing efficiency parameter μ_s . When the mass is fixed, varying the concentration changes r_s and ρ_s , and hence changes the lensing strength parameter μ_s . Because of the steep dependence on μ_s (panel a), small changes in the concentration can produce large changes in the Einstein radius and radial caustic. As a result, a 0.14 dex scatter in concentrations leads to a spread of some five orders of magnitude in the scale radii (panels d and e), or ten orders of magnitude in the lensing cross section ($\sigma_{\text{NFW}}^* \propto R_{\text{rc}}^2$).

In Figure 6 we have plotted the lensing cross section $\sigma_L(\log_{10} c)$, the Gaussian distribution of the concentration $\Phi(\log_{10} c)$, and their product. All curves are normalized to unity at $c = c_{\text{med}}$. The increase in the lensing cross section with concentration outweighs the decrease in the Gaussian tail out to 4 standard deviations. A peak occurs at around $\log_{10}(c/c_{\text{med}})/\sigma_{\log c} = 2$, where the product of σ_L and Φ is about two orders of magnitude larger than at c_{med} . The weighted cross section is given by the integral over this product ($\int \sigma_L \Phi d\log c / \int \Phi d\log c$), which explains the difference between a single NFW halo at $c = c_{\text{med}}$ and a distribu-

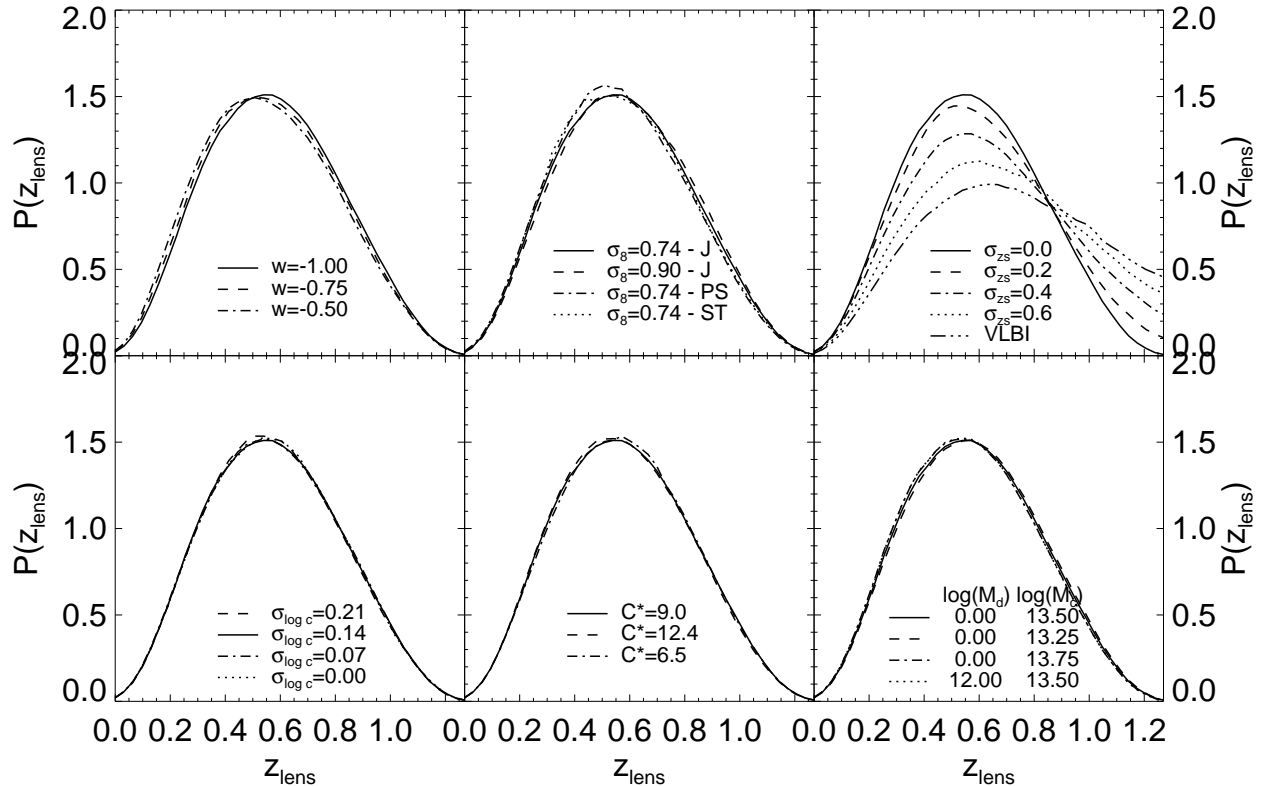


FIG. 4.— The effects of parameter variations on the normalized differential distribution of lens redshifts.

tion of NFW halos around this concentration with scatter equal to $\sigma_{\log c}$.

Put another way, even a massive halo with the median concentration has a relatively small Einstein radius and cross section, so if all halos have the median concentration ($\sigma_{\log c} = 0$) then wide-separation lenses will be quite rare. Only the most concentrated halos have reasonable cross sections for producing wide-separation lenses. Thus, wide-separation lenses are expected to be abundant only if the median and/or scatter in the concentration distribution is large enough to produce a sizable population of massive, concentrated halos. We conclude that it is imperative to include the distribution of concentrations in lens statistics calculations — and that the main limitation in predictions of wide-separation lenses will be uncertainties in \bar{c}_* and $\sigma_{\log c}$. These effects have been mentioned before (e.g., Keeton & Madau 2001; Wyithe, Turner, & Spergel 2001), but we were not previously aware that they could affect NFW lensing so dramatically.

4.6. Variation in M_d and M_c

The upper transition mass M_c parametrizes the change from galaxy-sized SIS to group- and cluster-sized NFW lenses, and its effect on the image separation distribution is orthogonal to the effects of the other parameters. Specifically, whereas the main effects discussed so far are increases or decreases in the abundance of wide-separation lenses, what M_c does is determine the po-

sition of the kink in the image separation distribution that marks the transition from normal to wide-separation lenses. For our fiducial value $\log M_c = 13.50$ the transition occurs at $\Delta\theta \approx 4''$, while for $\log M_c = 13.25$ it shifts down to $\Delta\theta \approx 3''$ and for $\log M_c = 13.75$ it shifts up to $\Delta\theta \approx 6''$. The lack of lenses with separations larger than $3''$ in the CLASS statistical sample makes it possible to place upper limits on M_c (see §5).

The lower transition mass M_d parametrizes the change from dwarf-sized NFW to galaxy-sized SIS lenses. Making M_d non-zero causes a drop in the abundance of lenses (in direct analogy with the galaxy to cluster transition at M_c). But the effects are not readily apparent in the image separation distribution, because they occur only at the smallest image separations. Except for very large values $\log M_d \sim 12$, the effect is confined to $\Delta\theta \lesssim 0''.1$. Because today's largest statistically complete lens sample is complete only above $0''.3$, the lower transition mass M_d is not well constrained by the available data (see §5 for details). For this reason we have chosen to omit the lower transition from our fiducial model.

Even more interesting are the effects of the transition masses on the time delay distribution. Increasing M_c effectively increases the abundance of lenses with intermediate separations $\Delta\theta \sim 4''$ – $6''$, which have long time delays; so it shifts the time delay distribution to higher values. Applying the M_d transition reduces the abundance of lenses with small separations, so it removes many of the lenses with short time delays and hence changes the

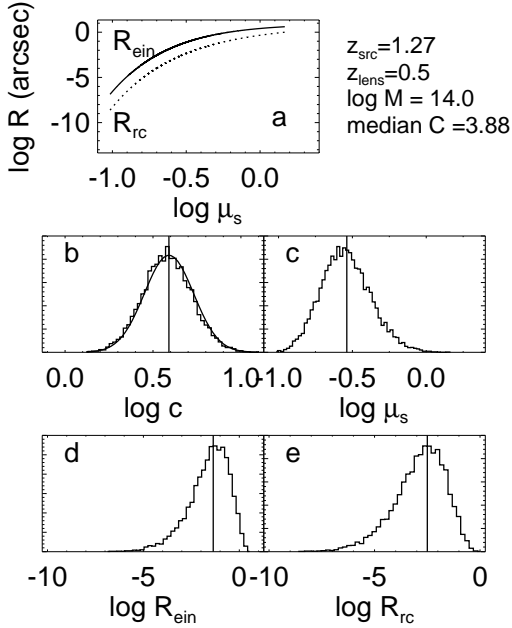


FIG. 5.— The change in the lensing properties of an NFW halo with concentration. (a) The strong dependence of the Einstein radius R_{ein} and the position of the radial caustic R_{rc} on the dimensionless lensing efficiency parameter μ_s . (b) A log-normal distribution of concentrations with width $\sigma_{\log c} = 0.14$ dex. The histogram shows the distribution of values drawn from the parent distribution represented by the smooth curve. (c–e) The resulting distributions of the efficiency parameter μ_s , the Einstein radius R_{ein} , and the radial caustic R_{rc} . The vertical lines indicate the values corresponding to the median concentration.

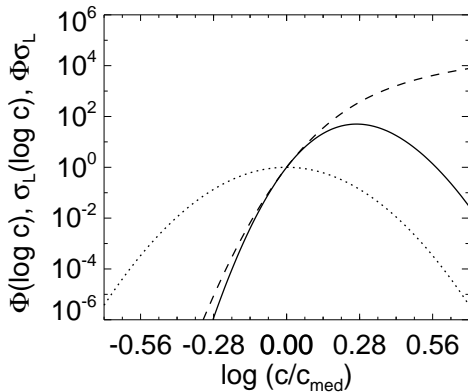


FIG. 6.— σ_L , the lensing cross section (dashed), Φ , a Gaussian distribution in $\log_{10}(c)$ with width $\sigma_{\log c} = 0.14$ dex (dotted), and the product of the two (solid), for the same lens-source system as in Figure 5. All curves have been normalized to unity at $c = c_{\text{med}}$. Since σ_L is a steeply rising function, the product of $\sigma_L \Phi$ peaks at around two standard deviations about the median, with a weighted cross section about two orders of magnitude larger than at c_{med} .

shape of the time delay distribution. Of all the parameter variations we consider, M_c and M_d have the most significant effects on the time delay distribution.

4.7. General comments

In previous analyses it was not clear whether lens statistics could simultaneously constrain both the cos-

mology and the profiles of massive dark matter halos. Our results suggest that the answer is yes, because of information contained in the distribution of lensed image separations (also see Huterer & Ma 2003). The abundance of wide-separation lenses depends primarily on σ_8 and the core properties of NFW halos (the distribution of concentrations; or equivalently, in generalized NFW models, the distribution of inner cusp slopes). The exact location of the break at $\Delta\theta \sim 4''$ between common arcsecond-scale lenses and less abundant wide-separation lenses probes baryonic cooling processes that determine why galaxies and clusters have different density profiles. The time delay distribution depends on these processes as well. Finally, the effects of w are seen at all image separations. Future data should therefore be able to break degeneracies between parameters by considering not only the total number of lenses but also the separation distribution.

5. COMPARISONS WITH THE JVAS/CLASS SURVEY

Already we can place constraints on some of the parameters using existing lens samples. The largest homogeneous sample comes from the combination of the Jodrell Bank/VLA Astrometric Survey (JVAS) and Cosmic Lens All-Sky Survey (CLASS), which in its entirety comprises VLA observations of 16503 radio sources with 22 multiply-imaged systems (Browne et al. 2002). A subset containing 8958 sources and 13 lenses forms a statistically complete sample with well-defined selection criteria (Myers et al. 2002). The survey is believed to be complete at $\Delta\theta \geq 0''.3$; the observed image separations range from $0''.33$ to $4''.55$ in the full sample, and $0''.33$ to $2''.57$ in the statistical subsample. The source redshift distribution is not well known, but the mean redshift of a subsample of sources is $\langle z_s \rangle = 1.27$ (Marlow et al. 2000).

In the range of angular separations probed by JVAS/CLASS the transition masses M_d and M_c are the most sensitive parameters. Variations in \bar{c}_* and $\sigma_{\log c}$ have larger effects overall, but only in the wide-separation tail where the null results of the JVAS/CLASS survey precludes interesting constraints. While Huterer & Ma (2003) claim to be able to distinguish different values of w and σ_8 using the CLASS statistical sample, we find that the effects of those parameters are smaller than the Poisson uncertainties. We therefore restrict attention to M_d and M_c .

For a statistical analysis of the *shape* of the image separation distribution, it seems reasonable to use all 22 lenses. The incompleteness of the full sample should not affect the normalized separation distribution. We quantify the agreement between our models and the data using the Kolmogorov–Smirnov (K.S.) test (e.g., Press et al. 1992, §14.3). The K.S. statistic is

$$D_{\text{KS}} = \max_{0 < \Delta\theta < \infty} |P_{\text{obs}}(< \Delta\theta) - P_{\text{mod}}(< \Delta\theta)|, \quad (23)$$

where $P_{\text{obs}}(< \Delta\theta)$ and $P_{\text{mod}}(< \Delta\theta)$ are the observed and predicted cumulative image separation distributions. Associated with D_{KS} is the K.S. probability $P_{\text{KS}}(D)$, quantifying the significance of an observed value of D as a disproof of the hypothesis that the data and the model represent the same distribution. Large values of D_{KS} correspond to small values of P_{KS} and indicate poor agreement between data and model.

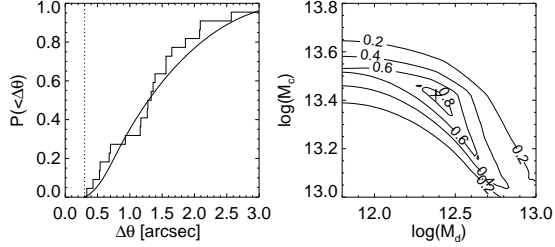


FIG. 7.— Comparison with JVAS/CLASS by K.S. test. The histogram on the left shows the normalized cumulative image separation distribution for all 22 lenses in the JVAS/CLASS sample. The solid line shows our best-fit model, determined by choosing M_d and M_c to minimize the K.S. measure D_{max} . The dotted vertical line indicates the JVAS/CLASS completeness limit, $\Delta\theta = 0''.3$. The right panel shows contours of P_{KS} with the maximum at $P_{\text{KS}} = 0.887$ marked by the cross.

Figure 7 shows contours of D_{KS} versus the transition masses M_d and M_c . The best fit (minimum value of D_{KS}) occurs at $\log M_d = 12.38$ and $\log M_c = 13.42$, and has a probability $P_{\text{KS}} = 88.7\%$. This value of the galaxy/cluster transition mass agrees well with the value found by Huterer & Ma (2003) from a similar analysis of the CLASS sample. The large inferred value of M_d is surprising; if taken at face value, it implies that even a relatively massive galaxy like the Milky Way is a “dwarf” whose density profile is NFW. It is not clear whether this result reflects a shortcoming of our theoretical modeling, or an unidentified selection effect in the JVAS/CLASS sample, or some other effect.

The K.S. test applies only to the shape of the image separation distribution and is insensitive to the total lensing probability. As a complementary approach, we use a χ^2 test to compare the unnormalized differential distributions; this test is somewhat less sensitive to the shapes of the distributions, but very sensitive to the relative normalizations. We take care to use only the statistically complete JVAS/CLASS subsample. We bin the 13 lenses into seven bins of width $\log \Delta\theta = 0.2$; although the two right-most bins are empty, we include them because our models can predict non-negligible numbers of lenses in this regime.

Figure 8 shows contours of χ^2 versus the transition masses. The best-fit model has $\chi^2 = 4.39$ for seven bins. We obtain good constraints on the upper transition mass M_c , with a best-fit value of $\log M_c = 13.46$ in good agreement with the results of the K.S. test. For M_d , by contrast, the χ^2 surface flattens into a long valley at $\log M_d < 12$. We are therefore unable to place a strong constraint on M_d . At 68% confidence level we can only place an upper bound of $\log M_d < 12.57$. As mentioned in §4.6, the effect of lowering M_d below $10^{12} M_\odot$ is confined to very small angular separations $\log \Delta\theta \lesssim -0.5$, outside of the range probed by JVAS/CLASS. Future surveys extending to smaller image separations will be needed to robustly constrain M_d .

We note that although our models produce an acceptable value of χ^2 , they cannot account for the sharp peak in the observed distribution at $\log \Delta\theta \sim 0''.2$. The presence of this peak actually explains why the K.S. test produces such a large best-fit value for M_d : being sensitive only to the shape of the separation distribution, the K.S.

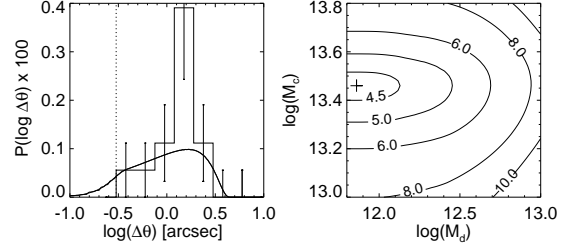


FIG. 8.— Comparison with JVAS/CLASS data by χ^2 test. The histogram on the left shows the unnormalized differential image separation distribution for the 13 lenses in the statistically complete JVAS/CLASS subsample. The error bars represent Poisson noise. The solid line shows our best-fit model, determined by choosing M_d and M_c to minimize χ^2 . The dotted vertical line indicates the JVAS/CLASS completeness limit for $\Delta\theta$. The right panel shows contours of χ^2 with the minimum marked by the cross.

test prefers to raise M_d to cause a rapid fall-off below the observed peak. Doing so sharply reduces the total lensing probability, however, and thus is disallowed by the χ^2 test. At this time it is not clear how to interpret these results, or even how to interpret the sharp peak in the observed distribution. Given that the sample size is still small and that even the high bin contains just seven lenses, it could just be due to a statistical fluctuation.

Nevertheless, the fact that we can reproduce the data so well without fine-tuning seems to validate our fiducial model.

6. FORECASTS

Although the JVAS/CLASS sample is small, ongoing and future surveys should dramatically increase the size of statistically complete lens samples and make it possible to constrain the model parameters. We can use our model to forecast the number of lenses that should be found in various surveys, and to understand when and how it may be possible to constrain the various model parameters. The most relevant surveys are deep, wide-field optical imaging surveys. The sources we consider are quasars, because they are common, distant, and straightforward to identify on the basis of optical colors (e.g., Croom et al. 2001; Richards et al. 2002). See Holz (2001), Goobar et al. (2002), and Oguri, Suto, & Turner (2003a) for estimates of the number of lenses in other populations, such as supernovae.

To compute the expected number of lensed quasars we must combine our calculated lensing probability with a description of the quasar population:

$$N_{\text{lens}} = \int dz \int dS \frac{dN_Q}{dz dS} P_{\text{lens}}(z, S), \quad (24)$$

where $dN_Q/dz dS$ is the distribution of quasars in redshift and flux, and P_{lens} is the lensing probability. We model the quasar population using the quasar luminosity function derived from the 2dF quasar redshift survey. Boyle et al. (2000) find that the luminosity function can be well described as a double power law, $\Phi \propto [(L/L_*)^\alpha + (L/L_*)^\beta]^{-1}$, where the power law indices are $\alpha = 3.41$ and $\beta = 1.58$ and the break magnitude evolves as $M_*(z) = M_*(0) - 3.4z + 0.68z^2$ for Λ CDM. While the 2dF quasar survey extends to redshift $z = 2.3$, we extrapolate the luminosity function

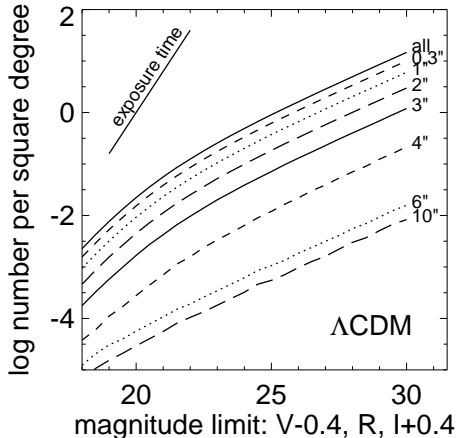


FIG. 9.— Predicted number counts of lensed quasars as a function of the survey limiting magnitude, for the fiducial model. The top curve depicts all lenses, and the remaining ones show lenses with image separations $\Delta\theta > 0.3, 1, 2, 3, 4, 6, 10$ arcsec (from top to bottom). The line in the upper left corner shows how the survey exposure time scales with limiting magnitude.

to $z \sim 5$. Deeper quasar surveys indicate a bright end slope $\alpha \approx 2.5$ at $z \sim 4$, suggesting that the pure luminosity evolution model may break down at high redshift (Fan et al. 2001). This should not significantly affect our results, however, because even at faint magnitudes no more than $\sim 10\%$ of the predicted lenses come from quasars at $z > 4$. To convert rest frame B-band luminosities to apparent magnitudes in various observed bands, we compute colors and K -corrections by convolving filter transmission curves with the composite quasar spectrum given by Vanden Berk et al. (2001). In the integral to compute the lensing magnification bias (see eqs. 6 and 14) we use the magnification of the fainter image, which is appropriate when we want to identify lenses where *both* images are above the flux limit.

Figure 9 shows our fiducial predictions for the number of lensed quasars per square degree, as a function of the R-band limiting magnitude of a survey, for a variety of cuts on the image separation. We have also computed the number counts for the V and I passbands. We find that these curves are very similar to those in Figure 9 but simply offset horizontally by approximately ± 0.4 mag; thus, we can use a single set of curves to determine the number counts in any of the three passbands.

An important qualitative result is that the lens number counts increase less rapidly than the exposure time as the depth increases. Making a survey 1 mag deeper increases the exposure time by a factor of 6.3 but only increases the number of lenses by a factor of ~ 1.7 – 3.3 (depending on the original depth). By contrast, keeping the same depth but increasing the area by a factor of 6.3 would increase the number of lenses by the same factor of 6.3. If the main goal of a survey is to find as many lenses as possible in a fixed amount of telescope time, then a wide area is more valuable than a deep limiting magnitude.

Figure 10 shows the predicted redshift distribution for lensed quasars. The distribution peaks at $z \sim 2.5$; it declines at low redshift mainly because the lensing optical depth becomes small, and at high redshift because

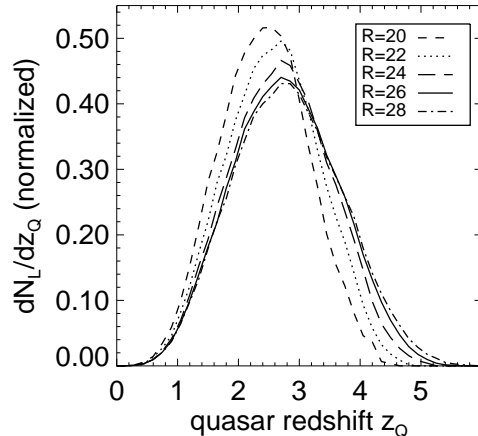


FIG. 10.— Predicted redshift distribution of lensed quasars. The different curves correspond to different R-band limiting magnitudes.

quasars become rare. The distribution shifts to slightly higher redshifts and becomes slightly broader at fainter limiting magnitudes, but the change is not large. Even at faint limiting magnitudes no more than 10% of the predicted lensed quasars have redshifts $z > 4$, so we believe that uncertainty in the quasar luminosity function at high redshift (whether the pure luminosity evolution model is viable at $z \gtrsim 4$) does not significantly affect our results.

Finally, Table 3 gives predictions for the number of lensed quasars in current and future imaging surveys, obtained by combining our predicted number counts with the surveys’ limiting magnitudes and areas. The systematic uncertainties are probably 10–20% for normal arcsecond-scale lenses, but much larger for wide-separation lenses (see §4). At present about 80 lenses are known, but the largest statistical sample is 13 radio lenses from CLASS. The ongoing, ground-based NOAO Deep Wide-Field Survey (Jannuzi & Dey 1999) and the Deep Lens Survey⁵ could each produce a sample as large as CLASS, or even larger if lenses smaller than $1''$ can be identified. The Sloan Digital Sky Survey by itself should more than double the number of lenses; several new SDSS lenses have already been discovered (e.g., Inada et al. 2003a, 2003b; Johnston et al. 2003). The proposed Supernova/Acceleration Probe (SNAP; Kim et al. 2002) satellite should discover a thousand or more lenses, and measure time delays for the several hundred discovered in the “deep” monitoring mode. The real breakthrough could come from the Large Synoptic Survey Telescope (Tyson et al. 2002), which would monitor 3/4 of the sky to reasonable depths and could discover some 10,000 lenses.

The search for lenses in these surveys will exploit the multiple colors that they all contain. Color cuts can be used to identify quasar candidates (e.g., Croom et al. 2001; Richards et al. 2002). Lens candidates can then be selected either as pairs of quasars separated by a few arcseconds, or as objects that have quasar colors but

⁵ See <http://dls.bell-labs.com>.

TABLE 3. SURVEY PREDICTIONS

Survey	Area (\square°)	Depth	Lensed Quasars			
			all	$>1''$	$>3''$	$>6''$
NOAO DWFS ^a	18	R = 25.8	26	11	2	0.03
DLS ^b	28	R \approx 26	45	19	4	0.1
SDSS ^c	10,000	$i^* = 20.2^c$	179	73	15	0.5
SNAP Deep ^d	15	I \sim 30	269	110	22	0.3
SNAP Wide ^d	300	I \sim 28	1,820	747	147	2
LSST ^e	30,000	R \sim 24	14,700	6,040	1,160	18

NOTE. — ^aNOAO Deep Wide-Field Survey (Jannuzi & Dey 1999); see <http://www.noao.edu/noao/noaodeep>.

^bDeep Lens Survey; see <http://dls.bell-labs.com>.

^cSloan Digital Sky Survey (e.g., Abazajian et al. 2003); see <http://www.sdss.org>. The SDSS magnitude limit is $i^* = 19.1$ for quasars at redshifts $z < 3$ and $i^* = 20.2$ for quasars at $z > 3$ (Richards et al. 2002).

^dSupernova/Acceleration Probe; see <http://snap.lbl.gov>. Current mission parameters include a “deep” mode with deep monitoring of $15 \square^\circ$, and a “wide” mode with shallower imaging of $300 \square^\circ$ (Kim et al. 2002).

^eLarge-aperture Synoptic Survey Telescope (Tyson et al. 2002); see <http://www.lsst.org>.

are marginally resolved (i.e., small-separation lenses in ground-based surveys). Such lens search techniques are being refined for large surveys by SDSS (Inada et al. 2003a; Pindor et al. 2003).

Spectroscopic confirmation of faint lens candidates may be difficult at present, although not with future 30-meter class telescope. Still, other confirmation methods are available. First, candidates with four (or more) lensed images can often be confirmed by the image configurations alone, and this should account for at least 25–30% and perhaps as many as 60% of the lenses (based on current predicted and observed 4-image to 2-image lens ratios; Keeton, Kochanek, & Seljak 1997; Rusin & Tegmark 2001). Second, surveys that include near-infrared imaging may discover infrared Einstein rings, which are lensed images of the quasar host galaxies that provide unambiguous evidence for lensing (e.g., Kochanek, Keeton, & McLeod 2001). Finally, monitoring programs like SNAP and LSST would offer the first chance to confirm lenses via time delays.

7. CONCLUSIONS

The statistics of strong gravitational lenses depend on a number of parameters related to both cosmology and the internal structure of the lenses. We have developed

the full formalism for computing lens statistics in universes dominated by quintessence. We have also shown how variations in the parameters lead to changes in the distribution of image separations, time delays, and lens redshifts. The strongest effects are found in the image separation distribution. Most lenses have image separations of around one arcsecond, corresponding to lensing by individual galaxies. In this regime, the most important parameters are w and σ_8 , which produce changes in the number of lenses at the tens of percent level. These effects are too small to be probed with existing lens surveys like CLASS (but see Huterer & Ma 2003), but will not be out of reach of the large samples that will be found with ongoing and future surveys.

The most dramatic parameter dependences are found among wide-separation lenses produced by groups and clusters of galaxies. The abundance of these lenses is extremely sensitive to the distribution of “concentration” parameters that describe the inner structure of massive dark matter halos, and somewhat less sensitive to the abundance of such halos. Wide-separation lenses will always be rare, but the remarkable sensitivity to the parameters means that even a small number of lenses with separations greater than $\sim 5''$ should yield interesting constraints. Indeed, the first instance of a wide-separation lens in a statistical sample has recently been discovered and is being analyzed for constraints on σ_8 and the core structure of cluster halos (Inada et al. 2003b; Oguri et al. 2003b).

Imaging surveys that are already underway will substantially increase the sample of strong lenses, and future surveys promise even more. Predicted samples of hundreds or thousands of lenses will revolutionize lens statistics, provided that their selection effects are well understood. A robust measurement of the distribution of image separations will yield internally self-consistent tests of cosmological parameters, the dark matter density profiles predicted by the popular cold dark matter, and the physics of baryonic cooling in massive halos.

We thank J. Frieman, M. Oguri, D. Rusin, and L. Strigari for interesting and helpful discussions. Support for this work was provided by NSF grant AST-0205738 (P.M.) and by NASA through Hubble Fellowship grant HST-HF-01141.01-A (C.R.K.) from the Space Telescope Science Institute, which is operated by the Association of Universities for Research in Astronomy, Inc., under NASA contract NAS5-26555.

APPENDIX

POWER SPECTRUM NORMALIZATION

We have normalized our power spectrum to match the observed abundance of galaxy clusters today. The largest and most recent X-ray flux-limited sample has been assembled by Reiprich & Böhringer (2002) and is known as HIFLUGCS. The cluster sample is based on the ROSAT All-Sky Survey and is composed of the brightest 63 clusters with galactic latitude $|b_{II}| \geq 20^\circ$ and flux $f_X(0.1 - 2.4 \text{ keV}) \geq 2 \times 10^{-11} \text{ ergs s}^{-1} \text{ cm}^{-2}$.

From the published data (Reiprich & Böhringer 2002) we have taken the cluster redshift (z), the flux in the energy range $0.1 - 2.4 \text{ keV}$ (f_X), and M_{200} , the mass enclosed in a region in which the average mass density is 200 times the critical density, and calculated an X-ray cluster mass function, analogous to the work by Reiprich & Böhringer (2002). The mass function was determined using the classical V_{max} method:

$$\frac{dn}{dM} = \frac{dN}{dV dM} = \frac{1}{\Delta M} \sum_{i=1}^N \frac{1}{V_{\text{max},i}}, \quad (\text{A1})$$

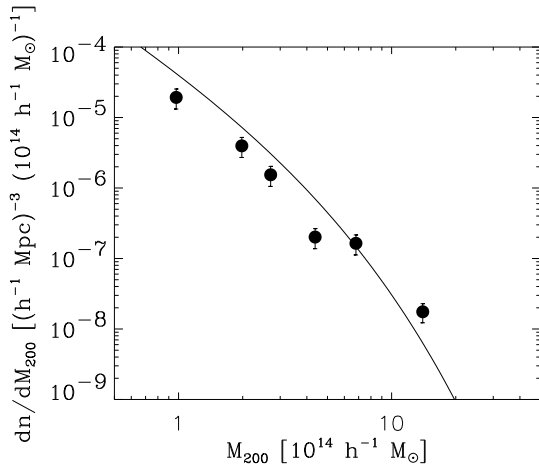


FIG. A11.— Λ CDM HIFLUGCS data and best-fit ($\sigma_8 = 0.74$) Jenkins et al. (2001) mass function.

where ΔM denotes the width of the mass bin, and $V_{\max,i} = V_{\max}(L_{X,i})$ is the maximum comoving volume within which the i^{th} cluster with luminosity $L_{X,i}$ could have been detected given the flux limit of the sample. Reiprich & Böhringer (2002) found a correlation between the total mass of the clusters and their X-ray luminosity, but with a significant scatter. An advantage of using $V_{\max}(L_X)$ in the calculation of the mass function is that this scatter is automatically taken into account.

There is a slight cosmology dependence of the mass function calculated this way, stemming from the use of the luminosity distance in converting f_X to L_X , but the effect is never larger than 5% and always smaller than the Poisson noise due to the limited number of clusters per bin.

The last step in the cluster normalization of the power spectrum is the matching of a theoretical mass function. As explained in § 3.5 we have chosen the Jenkins et al. (2001) mass function, which depends on the power spectrum through σ_M , see eqs. (20) and (22c). We simply performed a χ^2 minimization to find the value of σ_8 that produced the best-fit between the mass function and the HIFLUGCS X-ray cluster mass function. The $w = -1$ mass function and the best-fit mass function are shown in Figure A11. The w -dependence enters this method in two minor ways: the first is the aforementioned cosmology dependence of V_{\max} , and the second arises from the transfer function. Neither of these two effects is very significant, however, and so it is no surprise that the resulting σ_8 's are identical within uncertainties. We find $\sigma_8 = 0.738, 0.740$, and 0.742 for $w = -1, -0.75$, and -0.5 , respectively. The value $\sigma_8 = 0.74$ is consistent with what Reiprich & Böhringer (2002) found, who performed a more extensive analysis and found $\sigma_8 = 0.43\Omega_M^{-0.38}$, which evaluates to $\sigma_8 = 0.68$ for $\Omega_M = 0.3$. Note, however, that their full analysis prefers $\Omega_M = 0.12^{+0.06}_{-0.04}$ and $\sigma_8 = 0.96^{+0.15}_{-0.12}$.

REFERENCES

- Abazajian, K., et al. 2003, ApJ, submitted (astro-ph/0305492)
 Baccigalupi, C., Balbi, A., Matarrese, S., Perrotta, F., & Vittorio, N. 2002, PhRvD, 65, 063520
 Balbi, A., et al. 2000, ApJ, 545, L1
 Bartelmann, M. 1996, A&A, 313, 697
 Bartelmann, M., Perrotta, F., & Baccigalupi, C. 2003, A&A, 400, 19
 Blumenthal, G. R., Faber, S. M., Flores, R., & Primack, J. R. 1986, ApJ, 301, 27
 Browne, I. W. A., et al. 2002, MNRAS, 341, 13
 Bullock, J. S., Kolatt, T. S., Sigad, Y., Somerville, R. S., Kravtsov, A. V., Klypin, A. A., Primack, J. R., & Dekel, A. 2001, MNRAS, 321, 559
 Bullock, J. S., Kravtsov, A. V., Weinberg, D. H. 2002, ApJ, 539, 517
 Caldwell, R. R., Dave, R., & Steihaardt, P. J. 1998, PhRvL, 80, 1582
 Caldwell, R. R., Kamionkowski, M., & Weinberg, N.N. 2003, PhRvL, 91, 1301
 Chae, K.-H. 2002, MNRAS, in press (astro-ph/0211244)
 Chae, K.-H., et al. 2002, Phys. Rev. Lett., 89, 151301
 Cohn, J. D., Kochanek, C. S., McLeod, B. A., & Keeton, C. R. 2001, ApJ, 554, 1216
 Cooray, A. R., & Huterer, D. 1999, ApJ, 513, L95
 Croom, S. M., Smith, R. J., Boyle, B. J., Shanks, T., Loaring, N. S., Miller, L., & Lewis, I. J. 2001, MNRAS, 322, L29
 de Bernardis, P., et al. 2002, ApJ, 564, 559
 Efstathiou, G. 1999, MNRAS, 310, 842
 Eke, V. R., Navarro, J. F., & Steinmetz, M. 2001, ApJ, 554, 114
 Eisenstein, D. J., & Hu, W. 1999, ApJ, 511, 5
 Fabbiano, G. 1989, ARA&A, 27, 87
 Flores, R., & Primack, J. R., 1996, ApJ, 457, L5
 Frieman, J. A., Huterer, D., Linder, E. V., & Turner, M. S. 2002, PhRvD, 67, 3505
 Gerke, B. F., & Efstathiou, G. 2002, MNRAS, 335, 33
 Ghigna, S., Moore, B., Governato, F., Lake, G., Quinn, T. & Stadel, J. 2000, ApJ544, 616
 Goobar, A., Mörtzell, E., Amanullah, R., & Nugent, P. 2002, A&A, 393, 25
 Henstock, D.R., Browne, I.W.A., Wilkinson, P.N., & McMahon, R.G. 1997, MNRAS, 290, 380
 Holz, D. E. 2001, ApJ, 556, L71
 Huterer, D., & Turner, M. S. 2001, PhRvD, 64, 123527
 Huterer, D., & White, M. 2002, ApJ, 578, L95
 Huterer, D., & Ma, C.-P. 2003, ApJ, submitted (astro-ph/0307301)
 Inada, N., et al. 2003a, AJ, 126, 666
 Inada, N., et al. 2003b, Nature, submitted
 Jannuzi, B. T., & Dey, A. 1999, in Photometric Redshifts and the Detection of High Redshift Galaxies (ASP Conference Series, Vol. 191), ed. R. Weymann, L. Storrie-Lombardi, M. Sawicki, and R. Brunner, p. 111
 Jenkins, A., et al. 2001, MNRAS, 321, 372
 Jing, Y.P., & Suto, Y. 2000, ApJ, 529, L69
 Johnston, D. E., et al. 2003, AJ, submitted (astro-ph/0307371)
 Keeton, C. R. 1998, Ph.D. thesis, Harvard Univ.

- Keeton, C. R., Kochanek, C. S., & Seljak, U. 1997, *ApJ*, 482, 604
- Keeton, C. R., & Madau, P. 2001, *ApJ*, 549, L25
- Kim, A., et al. 2002, in *Survey and Other Telescope Technologies and Discoveries (Proceedings of the SPIE, Volume 4836)*, ed. J. A. Tyson & S. Wolff, p. 53
- Klypin, A., Maccio, A. V., Mainini, R., & Bonometto, S. A. 2003, *ApJ*, submitted (astro-ph/0303304)
- Kochanek, C. S. 1995, *ApJ*, 453, 545
- Kochanek, C. S., Keeton, C. R., & McLeod, B. A. 2001, *ApJ*, 547, 50
- Kochanek, C. S., & White, M. 2001, *ApJ*, 559, 531
- Komatsu, E., & Seljak, U. 2002, *MNRAS*, 336, 1256
- Koopmans, L. V. E., & Treu, T. 2003, *ApJ*, 583, 606
- Li, L.-X., & Ostriker, J. P. 2002, *ApJ*, 566, 652
- Linder, E. V., & Jenkins, A. 2003, */mnras*, in press (astro-ph/0305286)
- Ma, C.-P., Caldwell, R. R., Bode, P., & Wang, L. 1999, *ApJ*, 521, L1
- Ma, C.-P. 2003, *ApJ*, 584, L1
- Marlow, D. R., Rusin, D., Jackson, N., Wilkinson, P. N., & Browne, I. W. A. 2000, *AJ*, 119, 2629
- Moore, B., Quinn, T., Governato, F., Stadel, J., & Lake, G. 1999, *MNRAS*, 310, 1147
- Myers, S., et al. 2002, *MNRAS*, 341, 13
- Narayan, R., & White, S. D. M. 1988, *MNRAS*, 231, P97
- Navarro, J. F., Frenk, C. S., & White, S. D. M. 1997, *ApJ*, 490, 493
- Oguri, M., Taruya, A., Suto, Y., & Turner, E. L. 2002, *ApJ*, 568, 488
- Oguri, M., Suto, Y., & Turner, E. L. 2003, *ApJ*, 583, 584
- Oguri, M., et al. 2003b, in preparation
- Padmanabhan, T. 2003, *Physics Reports*, 380, 235 (also: hep-th/0212290)
- Peebles, P. J. E., & Ratra, B. 1988, *ApJ*, 325, L17
- Perlmutter, S., et al. 1999, *ApJ*, 517, 565
- Perlmutter, S., Turner, M. S., & White, M. 1999, *PhRvL*, 83, 670
- Pindor, B., Turner, E. L., Lupton, R. H., & Brinkman, J. 2003, */aj*, 125, 2325
- Porciani, C., & Madau, P. 2000, *ApJ*, 532, 679
- Press, W. H., & Schechter, P. 1974, *ApJ*, 187, 425
- Press, W. H., Teukolsky, S. A., Vetterling, W. T., & Flannery, B. P. 1992, *Numerical Recipes in C*, 2nd ed. (Cambridge: Cambridge Univ. Press)
- Pryke, C., Halverson, N. W., Leitch, E. M., Kovac, J., Carlstrom, J. E., Holzappel, W. L., & Dragovan, M. 2002, *ApJ*, 568, 46
- Reiprich, T. H., & Böhringer, H. 2002, *ApJ*, 567, 716
- Richards, G. T., et al. 2002, *AJ*, 123, 2945
- Riess, A. G., et al. 2001, *ApJ*, 560, 49
- Rix, H.-W., de Zeeuw, P. T., Carollo, C. M., Cretton, N., & van der Marel, R. P. 1997, *ApJ*, 488, 702
- Rusin, D., Kochanek, C. S., & Keeton, C. R. 2003, *ApJ*, 595, 29
- Rusin, D., & Tegmark, M. 2001, *ApJ*, 553, 709
- Sarbu, N., Rusin, D., & Ma, C.-P. 2001, *ApJ*, 561, L147
- Sheth, R. K., & Tormen, G. 1999, *MNRAS*, 308, 119
- Silveira, V., & Waga, I. 1994, *PhRvD*, 50, 4890
- Spergel, D. N., et al. 2003, *ApJS*, 148, 175
- Springel, V., & Hernquist, L. 2003, *MNRAS*, 339, 289
- Steinhardt, P. J., Wang, L., & Zlatev, I. 1999, *PhRvD*, 59, 123504
- Treu, T., & Koopmans, L. V. E. 2003, *ApJ*, 583, 606
- Turner, E. L., Ostriker, J. P., & Gott, J. R., III 1984, *ApJ*, 284, 1
- Tyson, J. A., et al. 2002, in *Survey and Other Telescope Technologies and Discoveries (Proceedings of the SPIE, Volume 4836)*, ed. J. A. Tyson & S. Wolff, p. 10
- Waga, I., & Frieman, J. A. 2000, *PhRvD*, 62, 043521
- Wang, L., Caldwell, R. R., Ostriker, J. P., & Steinhardt, P. J. 2000, *ApJ*, 530, 17
- Wang, L., & Steinhardt, P. J. 1998, *ApJ*, 508, 483
- Wechsler, R.H., Bullock, J.S., Primack, J.R., Kravtsov, A.V., Dekel, A. 2002, *ApJ*, 568, 52
- Weinberg, , N. N., & Kamionkowski, M. 2002, *MNRAS*, 341, 251
- Wyithe, J. S. B., Turner, E. L., & Spergel, D. N. 2001, *ApJ*, 555, 504
- Zhao, H. S. 1996, *MNRAS*, 278, 488
- Zhao, D. H., Mo, H. J., Jing, Y. P., Börner, G. 2003, *MNRAS*, 339, 127
- Zhao, D. H., Jing, Y. P., Mo, H. J., & Börner, G. 2003, *ApJ*, in press (astro-ph/0309375)